crystals

MDPI

Article

Fabrication of AlZn4SiPb/Steel Clad Sheets by Roll Bonding: Their Microstructure and Mechanical Properties

Pengju Wang [1,2], Ning Zhong [2], Liyue Tu [2], Weiming Hong [2], Yanming Lv [2], Yonghong Chen [2], Jian Sun [2], Caiyong Luo [2], Zejun Chen [3] and Qian Tang [1,*]

[1] College of Mechanical and Vehicle Engineering, Chongqing University, Chongqing 400030, China
[2] Chongqing Yuejin Machinery Co., Ltd., Chongqing 402160, China
[3] College of Materials and Engineering, Chongqing University, Chongqing 400030, China
* Correspondence: tqcqu@cqu.edu.cn

Abstract: An AlZn4SiPb/steel clad composite was prepared via roll bonding at room temperature. The influence of solution and aging treatment on the structure and performance of the clad composite was investigated. The results show that the Al/steel clad composites exhibited satisfactory interfacial adhesion. Pb of the aged Al matrix was spheroidized and uniformly dispersed. An uneven interfacial transition area with a thickness of 30–150 nm was observed for the aged sample. Some rod-shaped nanoscale β' phases occurred in the aged Al matrix. After the solution and aging treatment, the steel layer recovered, and the γ-fibre texture increased. The tensile strength for individual Al alloy layer improved. The yield ratio of the aged clad sheet was lower than that of the initial sample. The tensile strength values of the composites were consistent with the computed values from the rule of mixture. The interfacial bonding strength of the initial sample was 70 MPa; the aged sample greatly improved and reached 130 MPa in strength.

Keywords: rolling bonding; clad sheet; solution and aging treatment; microstructure; mechanical properties

check for updates

Citation: Wang, P.; Zhong, N.; Tu, L.; Hong, W.; Lv, Y.; Chen, Y.; Sun, J.; Luo, C.; Chen, Z.; Tang, Q. Fabrication of AlZn4SiPb/Steel Clad Sheets by Roll Bonding: Their Microstructure and Mechanical Properties. *Crystals* **2023**, *13*, 292. https://doi.org/10.3390/cryst13020292

Academic Editor: Leonid Kustov

Received: 28 December 2022
Revised: 2 February 2023
Accepted: 6 February 2023
Published: 9 February 2023

Copyright: © 2023 by the authors. Licensee MDPI, Basel, Switzerland. This article is an open access article distributed under the terms and conditions of the Creative Commons Attribution (CC BY) license (https://creativecommons.org/licenses/by/4.0/).

1. Introduction

An Al-based bearing alloy is widely used as a substitute for Cu-Sn-Pb conventional bearing material due to its good bearing and mechanical properties, as well as its reduced use of copper. Multiple Al-based bearing materials have been explored in recent decades [1]. An Al-Sn alloy has good anti-friction properties due to the presence of the soft Sn. However, the Al-Sn alloy struggles to support heavy loads, which is a problem following more stringent requirements for the manufacturing of engines. An Al-Zn alloy is a logical alternative due to its high fatigue resistance and load capacity [2,3].

To further improve the fatigue strength and carrying ability of the sliding bearing, an Al alloy was bonded with low-carbon steel [4]. Many methods were used to attain the interfacial bonding between Al and steel layers, such as roll bonding, diffusion welding, explosion welding and friction stir bonding. Compared to other methods, roll bonding is productive, universal, and convenient [5–8]. Therefore, roll bonding is an appropriate method for the large-scale manufacture of Al/steel clad sheets and strips.

Recently, Al/STS clad sheets and strips have been widely researched. Fu et al. [9] fabricated some Al/STS clad sheets via roll bonding and found that the oxidation treatment of a steel surface enormously enhanced Al/STS interfacial bonding strength. The surface of steel can also be treated via the deposition of electrochemical coatings [10,11]. Chen et al. [12] produced thicker Al/Al/STS clad composites via two rolling processes at different temperatures. In this study, the pull-off strength of Al/steel interface reached 110 MPa, and the shear strength of Al/steel interface surpassed 70 MPa. Filho et al. [13] explored the influence of the interfacial shear mode on the shear strain zone in the Al/STS roll bonding

process. They concluded that the shear zone between Al and steel layers was mainly related to the scale of the shear strain and the structural composition of the different metals. Kim et al. [14] explored the interfacial bonding strength and shear stress of cold-rolled and annealing Al1050/STS439 clad sheets using the finite element method. Chen et al. [15] explored the influence of multiple array methods between the rolling reduction and heat treatment on the interfacial diffusion of twin-roll cast Al/steel composites. A high rolling reduction could reduce the incubation period of interfacial intermetallic compounds after annealing at 510 °C for 1.5 h. However, previous studies primarily explored pure-Al and low-carbon-steel composites, and the influence of the solution and aging treatment on the structure and mechanical performance of Al alloy/low-carbon-steel composites remains unclear.

In the present study, the AlZn4SiPb/steel clad composite was successfully produced using a roll bonding method during room temperature. The microstructures of Al/steel interface and matrix metals were explored via scanning electron microscopy (SEM), transmission electron microscopy (TEM), and electron backscatter diffraction (EBSD). Effects of the solution and aging treatment on the mechanical performance were explored.

2. Materials and Methods

The original materials of the composite are an AlZn4SiPb alloy (2.2 mm in thickness) and low-carbon steel (3.2 mm in thickness). Tables 1 and 2 show the chemical compositions of the two sheets, respectively. To reduce the deformation resistance of materials, the AlZn4SiPb sheets were heat-treated at a temperature of 350 °C for 0.5 h, and the low-carbon steel sheets were heat-treated at a temperature of 600 °C for 2 h. Al and steel sheets of 100 mm in width and 120 mm in length were used as the original size.

Table 1. Chemical constitutions of AlZn4SiPb sheet (wt.%).

	Al	Zn	Si	Mg	Cu	Fe	Ti
AlZn4SiPb	Bal.	4.45	1.21	0.49	0.89	0.03	0.12

Table 2. Chemical constitutions of steel sheet (wt.%).

	Fe	C	Si	Mn	P	S
Steel	Bal.	0.09	0.25	0.30	0.03	0.03

The surfaces of AlZn4SiPb alloy were treated using a wire brush with the rotational speed of 180 r/s and 95 mm in diameter. The low-carbon steel was cleaned using a flap disc (rotational speed of 180 r/s; diameter of 90 mm) constituted by the abrasive band of 60#. Then, the metal was immersed in ethyl alcohol for 30 min to remove the residual grease and immediately dried using a hair dryer. To reduce the mismatch of Al alloy and steel during the production, the materials were punched in the front end and fixed by an aluminium rivet. The riveted AlZn4SiPb/steel sheets were pushed into the laboratory mill and rolled at room temperature. A thickness reduction of 58% was achieved at a rolling speed of 12 m/min. Subsequently, the composite was heat-treated at 350 °C for a holding time of 1 h. This was a general heat treatment for the clad sheets of the sliding bearing. The clad sheets then returned to their initial state. To improve their mechanical properties, the solution annealing of the initial clad sheets was performed at 470 °C for 1 h, followed by rapid cooling. Then, the clad sheets were aged in an oil bath furnace at a temperature of 120 °C for a holding time of 24 h. The manufacturing and preparation process of AlZn4SiPb/steel clad composite is presented in Figure 1.

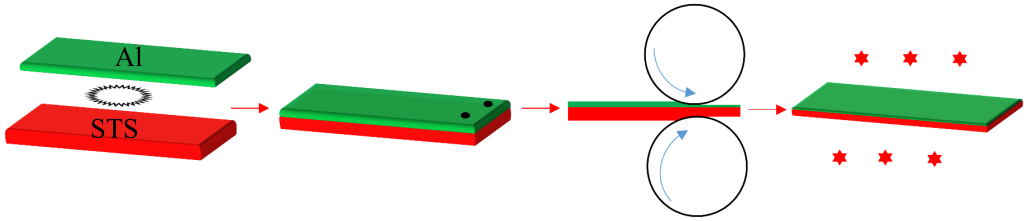


Figure 1. Diagrammatic drawing of the manufacturing and preparation process for AlZn4SiPb/steel clad composites.

The samples were prepared by wire-electrode cutting 10 mm in RD direction and 8 mm in ND direction for the microstructure analysis. Next, the sample was ground using 600#, 1000#, 2000#, and 4000# abrasive papers and polished using a diamond polishing paste 3 μm in diameter. The interface and microtexture were tested using field emission SEM (TSCAN MIRA 3) with the EBSD and EDS detectors.

To remove the surface stress caused by abrasive papers and diamond polishing paste, samples for EBSD were prepared using electro-polishing. For the Al layer, the electrolyte used in this experiment was a mixture of perchloric acid and ethyl alcohol (1:9), and the polishing process was carried out at a voltage of 20 V for 40 s at room temperature. For the steel layer, the electrolyte was a mixture of perchloric acid, water, and ethyl alcohol (2:3:20), and the polishing process was conducted at the voltage of 30 V for 20 s at the temperature of −20 °C.

Sampling for TEM observation was carried out using a focused ion beam (FIB Zeiss Auriga). Firstly, the sample was mechanically polished by abrasive papers and a diamond polishing paste. Then, a rough block perpendicular to the Al/steel interface was cut and milled using a Ga^+ ion with a voltage of 20 kV. Finally, for the TEM observation, the thinning and cleaning of the piece were conducted at a voltage of 3 kV [5]. The microstructure of piece, with an acceleration voltage of 200 kV, was characterized via the TEM (FEI Tecnai G2 F20).

To explore the influence of solution and aging treatment on the mechanical properties, a tensile test and a tensile shear test were executed on the Shimadzu universal testing machine with a tensile speed of 1 mm/min. Figure 2 exhibits the schematic figures of tensile shear test and tensile test for the clad composites. To validate the strength theory of the composites, tensile samples of Al and steel layers were mechanically cut from the Al/steel clad sheets and independently used to test mechanical performance.

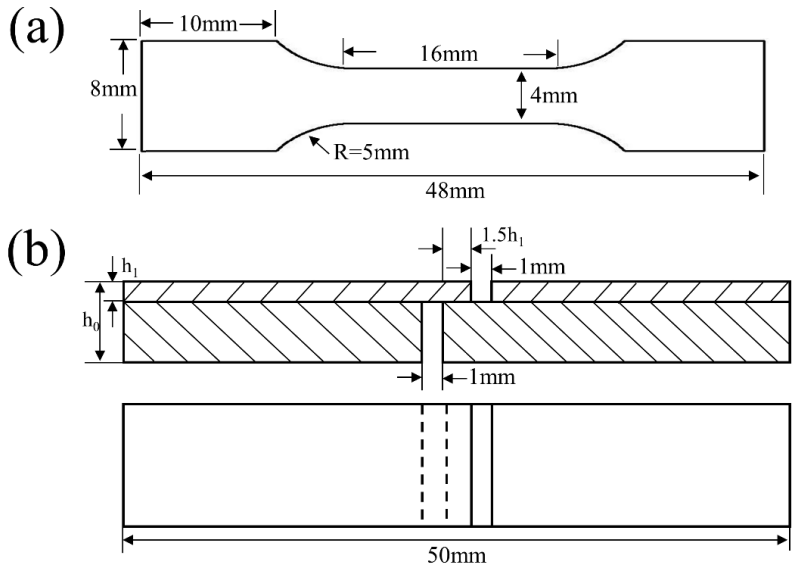


Figure 2. Schematic figure of (**a**) tensile test and (**b**) tensile shear test.

3. Results and Discussion

3.1. Microstructure of AlZn4SiPb/Steel Clad Sheets

Figure 3 shows the back-scattered electrons (BSEs) and element line scanning of the initial and aged Al/steel interfaces. There were no evident cracks or faults at the Al/steel interfaces, indicating that bonding interfaces were intact. It was observed that the Pb phase was elongated along the rolling direction towards the white Pb ribbon, as shown in Figure 3a. When the sample solution was annealed at 470 °C, the white Pb phase of the Al layer spheroidized and was uniformly distributed, as shown in Figure 3b. The lack of a significant change in the width of EDS line scanning suggested that no evident atomic diffusion zone was produced at the aged Al/steel interface.

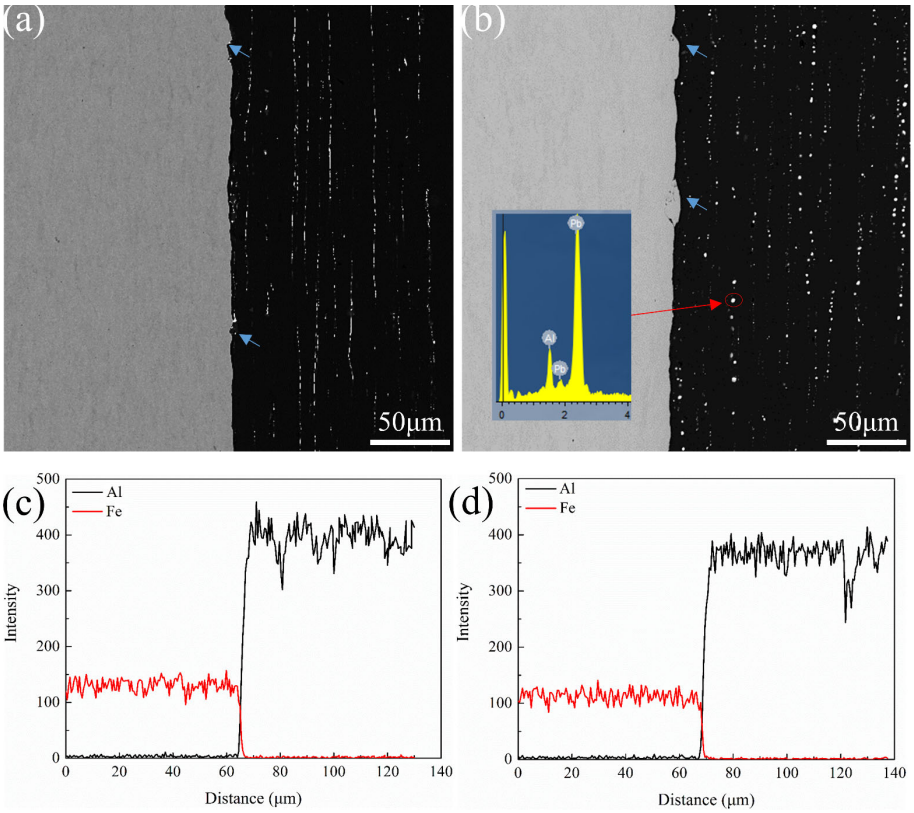


Figure 3. Interfacial images of Al/steel composites: (**a**) initial sample, (**b**) aged sample, (**c**) SEM-EDS line scan of (**a**), and (**d**) SEM-EDS line scan of (**b**).

As shown in the phase diagram of the Al-Pb binary system, the solid solubility of Pb element in Al was 1.2% at the monotectic temperature of 658 °C, and the value was nearly zero at room temperature [16]. Therefore, Pb was mainly distributed at the grain boundary of the α-Al alloy. In the roll bonding process, softer Pb was elongated along the rolling direction towards the white Pb ribbon under rolling pressure. The Pb metal had a lower melting point of 327.46 °C. When the samples were annealed at a higher temperature, the Pb melted, migrated, and turned into a ball. Moreover, the dispersion distribution of the globular Pb phase was good for the anti-friction and anti-wear of the sliding bearing [17].

Some small "sawtooth" gaps (indicated by the blue arrows in Figure 3a,b), which had a similar shape to the Great Wall of China, were observed in the Al/steel bonding interfaces. As mentioned in the method, the surfaces of original materials were mechanically treated via the wire brush and flap disc before roll bonding. The wire brush and flap disc were able to eliminate the surface defects and produce work-hardening surfaces for the original Al and steel sheets. During roll bonding, the work-hardening layers of the two sheets fractured, and then the virginal Al and steel metals were forced out from the gaps. The Al

and steel metals were close to each other and tightly combined. This confirmed the film theory for the bonding mechanism of clad sheets [18].

To explore the interfacial microstructure, a TEM analysis was performed for the aged sample. The TEM bright-field picture of the Al/steel interface region and the EDS line distribution of the elements (Al and Fe) are shown in Figure 4. No microvoids or cracks at the Al/steel interface were observed, as shown in Figure 4a. An uneven transition area (marked by the blue arrows) with a thickness of 30–150 nm formed between the Al and steel layers in Figure 4b. A significant atom diffusion layer was observed, as shown in Figure 4c. The atom diffusion rate mainly depended on the diffusion coefficient, K. A diffusing coefficient of Fe atoms in the Al alloy at 470 °C was $K = 4.32 \times 10^{-10}$ cm^2/s [19]. The distance of diffusion zone, L, was mainly related to the holding time and diffusing coefficient: $L = (Kt)^{0.5}$ [5,20]. The calculated value of the diffusion distance was 124 nm.

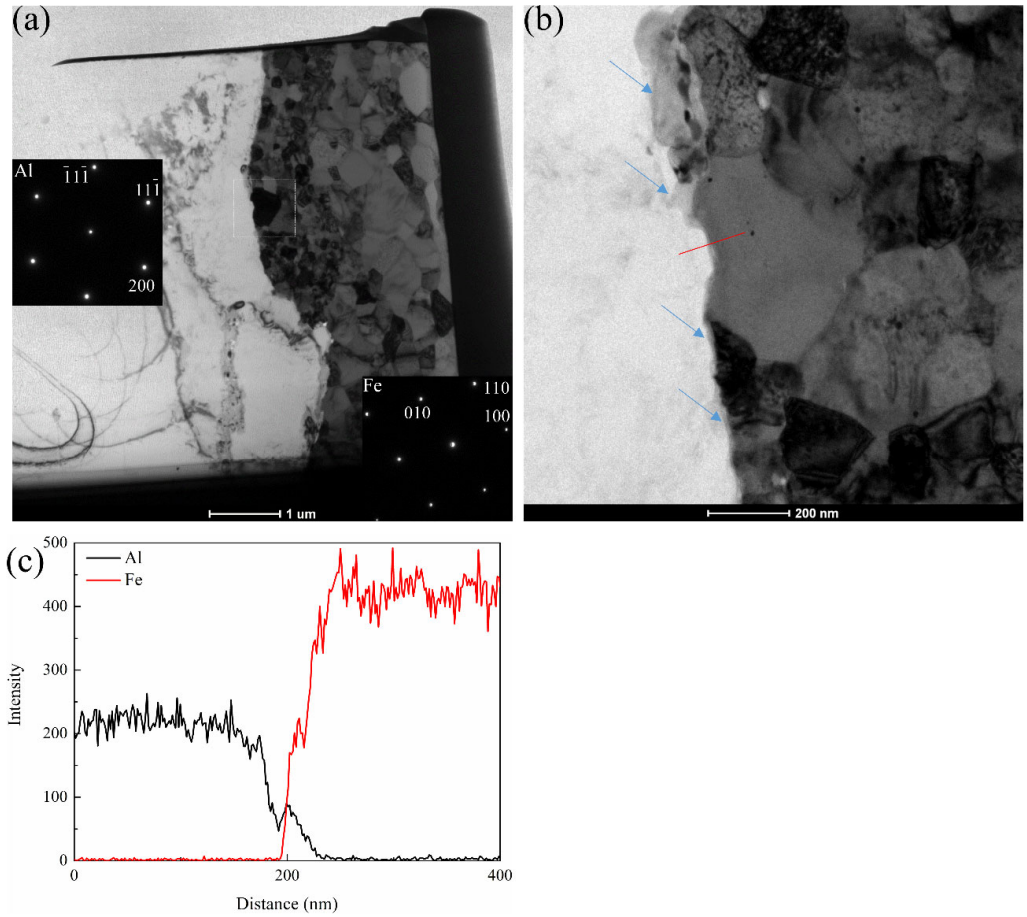


Figure 4. (**a**) TEM bright-field picture of the Al/steel bonding interface of the aged sample, (**b**) amplified interfacial structure from the dashed rectangle in (**a**), and (**c**) the EDS line scanning from the red line in (**b**).

The interfacial bonding mechanism indicated that the fresh metals were squeezed out of the surface cracks and made contact with each other. Therefore, there were two contact points in the Al/steel interface zone, one of which was the surface layer of the material that made contact with the fresh metal. It was known that the mechanical preparation of the surface would produce massive crystal defects on the surface of the sheet. When the solution temperature was 470 °C, the defects provided the diffusion channel and abundant energy for the atomic migration of the Al and Fe. The diffusing distance was greater than the calculated value. The other contact point was the fresh metal with the fresh metal. Due to fewer crystal defects on this zone, the Al and Fe atoms required an incubation period to generate enough energy and achieve diffusion. Therefore, the diffusion distance was

less than the calculated value. This explained why the uneven transition occurred at the Al/steel interface.

Figure 5 shows the TEM bright-field picture of the aged Al alloy and the mapping images of the atoms. It was observed that some rod-shaped, fine nanoscale phases occurred in the aged Al alloy. The relevant SAED pattern of the [001] zone axis indicated that this phase was β' (Mg_9Si_5). It was hexagonal, with a = 7.05 Å and c = 4.05 Å [21]. However, the material of AlZn4SiPb was Al-Zn matrix alloy, and the precipitation phases should be η' ($MgZn_2$) after the solution and aging treatment [22]. This was mainly related to the formation enthalpy (ΔH) of the atomic cluster. The $\Delta H_{Mg\text{-}Si}$ value was −16.4 kJ/mol, far below the $\Delta H_{Mg\text{-}Zn}$ value of −6.1 kJ/mol [23]. Therefore, from the perspective of energy generation, precipitation mainly focused on the Mg-Si phase.

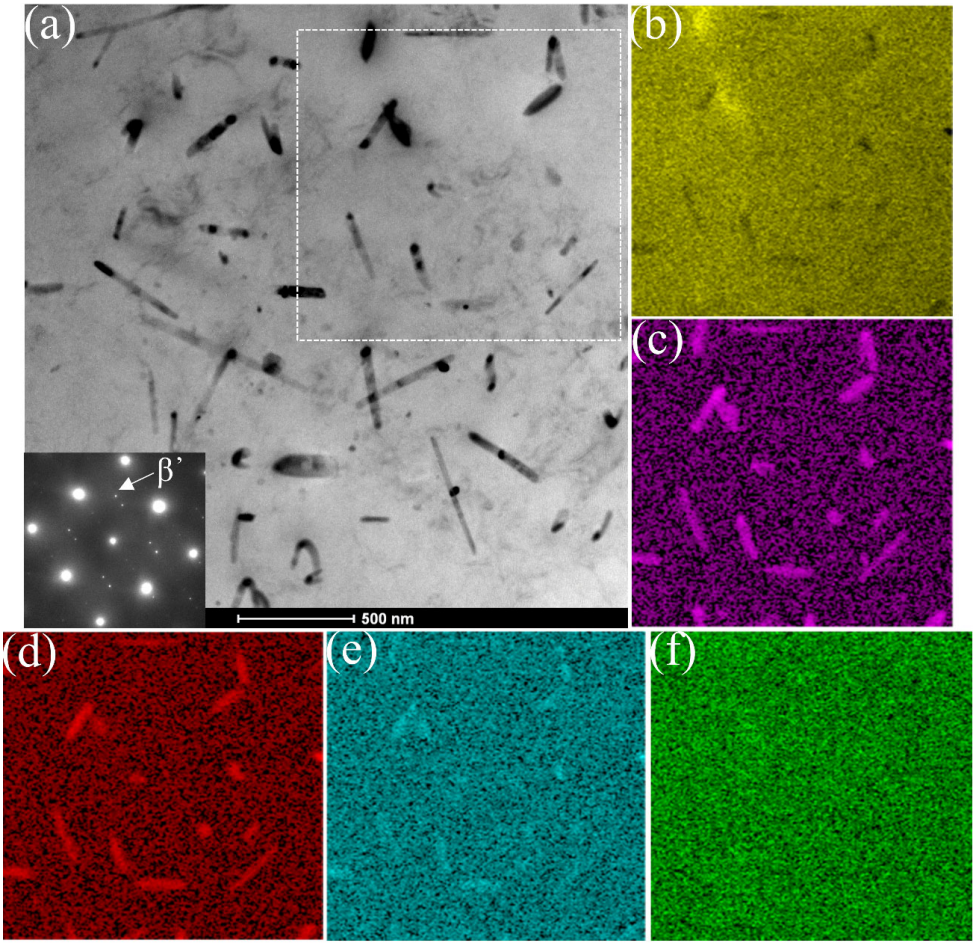


Figure 5. TEM bright-field picture of the aged Al alloy, (**b**–**f**) the mapping images of the atoms (Al, Si, Mg, Cu, and Zn) for the white dashed rectangle in (**a**).

From the result of TEM-EDS mapping in Figure 5, the rod-shaped precipitate consisted of Al, Si, Mg, and Cu. During the aging process, the following precipitation sequence for the Al-Mg-Si-Cu alloy occurred: supersaturated solid solution (SSSS)-atomic clusters-GP zones-β''-β', Q'-β, Q [24]. The Q phase consisted of Al, Mg, Cu, and Si elements. Compared with the Al-Mg-Cu-Si alloy, due to the lower solution and aging temperature used in this study, the aged sample lacked sufficient energy to form the Q phase [25]. The influence of the higher solution and aged temperature on the structure and mechanical performance of the AlZn4Sib alloy will be explored in future research.

Figure 6a–d show the IPFs of AlZn4SiPb and steel layers for the initial and aged AlZn4SiPb/steel clad sheets. Recrystallized grains of different sizes were observed, as shown in Figure 6a. This phenomenon was related to the lower annealing temperature of

the initial sample. When annealing was carried out at a higher temperature, the difference in the grain sizes decreased. Because of the Pb phase, a black unidentified zone was observed in the IPFs of the Al layer. It is worth noting that the unidentified zone in the initial sample was larger than that in the aged sample. Compared with the globular Pb, the Pb ribbon formed a larger unidentified zone in the initial sample. Moreover, some precipitation of the Al alloy was dissolved when the sample was annealed at the solution temperature of 470 °C. Therefore, the Al layer of the aged sample has a smaller unidentified zone.

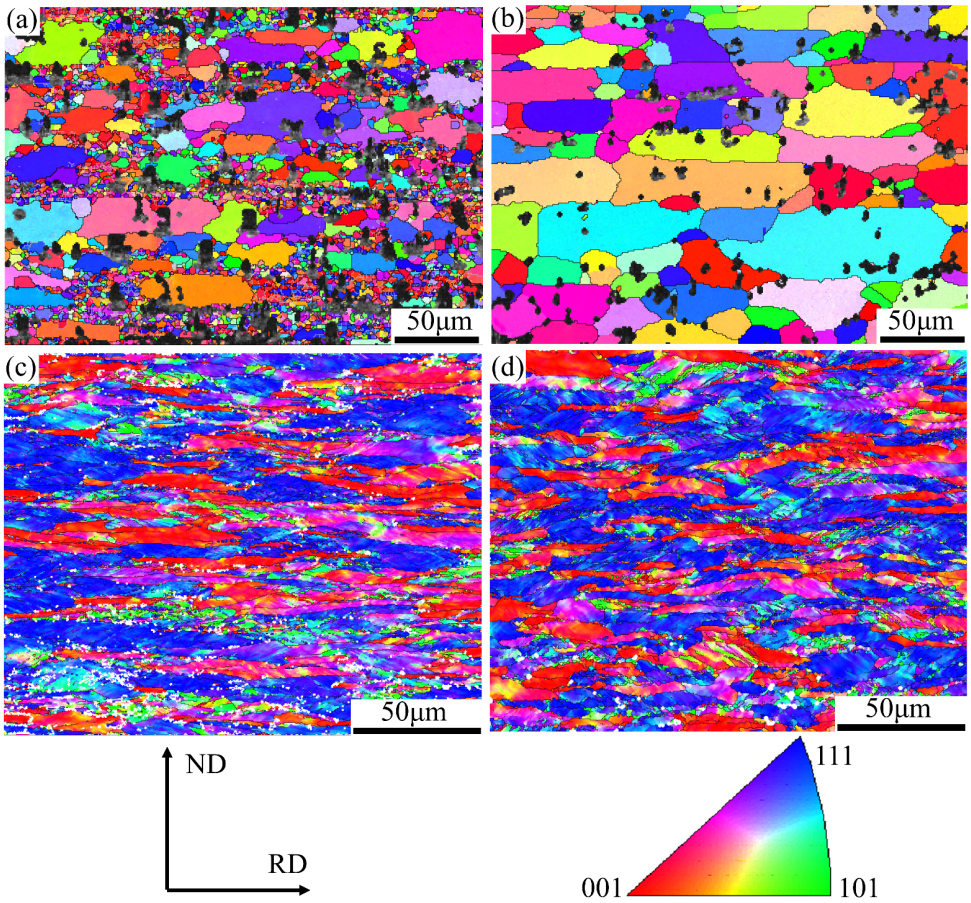


Figure 6. Inverse pole figures (IPFs) of samples: (**a**) initial Al layer, (**b**) aged Al layer, (**c**) initial steel layer, and (**d**) aged steel layer.

As shown in Figure 6c–d, the IPFs of the steel layers have a deformed microstructure. The grain of steel layer was extended along with the roll forming direction. Due to the higher recovery and recrystallization temperature, the aged sample still exhibited a rolling microstructure. The low-angle grain boundary (2°–15°), which contained numerous dislocations, represents the deformation degree of the materials. The value of the initial sample was 60%, and the value of the aged sample was 52%. Therefore, the solution treatment decreased the density of the dislocation and promoted the recovery of the steel layer. However, some fine grains of approximately 50–500 nm were observed at the steel side of the aged Al/steel interface in Figure 4a. The surface layer of the steel sheet was not only affected by the crushing force of the flap disc, but also suffered from friction shear and rolling pressure. The surface-stored energy produced by the drastic plastic transformation promoted the nucleation and growth of grains. Therefore, some small grains formed at the steel side of the aged Al/steel interface.

Figure 7 shows the $\varphi_2 = 45°$ section on the orientation distribution function (ODF) maps of steel layer. The main α-fibre (<110>//RD, including important components {001}<110>, {112}<110> and {111}<110>) and γ-fibre (<111>//ND, including major components {111}<112> and {111}<110>) texture members were observed.

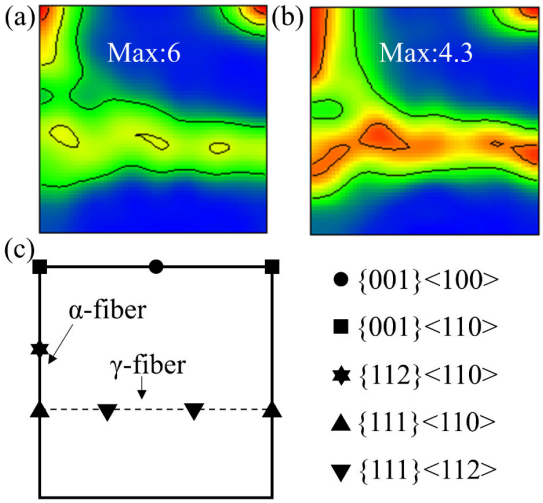


Figure 7. The $\varphi_2 = 45^\circ$ sections in orientation distribution function (ODF) maps of the steel layers: (**a**) initial sample, (**b**) aged sample, and (**c**) the typical positions of the main textures.

It was previously known that the α-fibre and γ-fibre textures formed the typical orientation of cold rolling ferritic steel [26]. During the rolling process, the steel layer went through a drastic deformation and formed cold rolling textures. Compared with the initial sample, the α-fibre texture of the aged sample worsened, and the γ-fibre texture improved. This was mainly related to the recovery of the steel. Moreover, the γ-fibre texture can improve the deep drawing performance of low-carbon steel [27].

3.2. Tensile Properties of AlZn4SiPb/Steel Clad Sheets

As shown in Figure 8, the engineering stress–strain curves of the individual metal sheets and Al/steel composites were measured. The mechanical properties were ultimate tensile strength (UTS), yield strength (YS), and elongation (EL). Table 3 shows the corresponding values of the curves. Compared with the initial clad composites, the UTS and TS of the aged composites and steel sheets reduced, and elongation improved. It was noted that the aged Al alloy had better mechanical properties than those of the initial sample. The fine Mg-Si phases contributed to the improvement of the aged Al alloy, as shown in Figure 5.

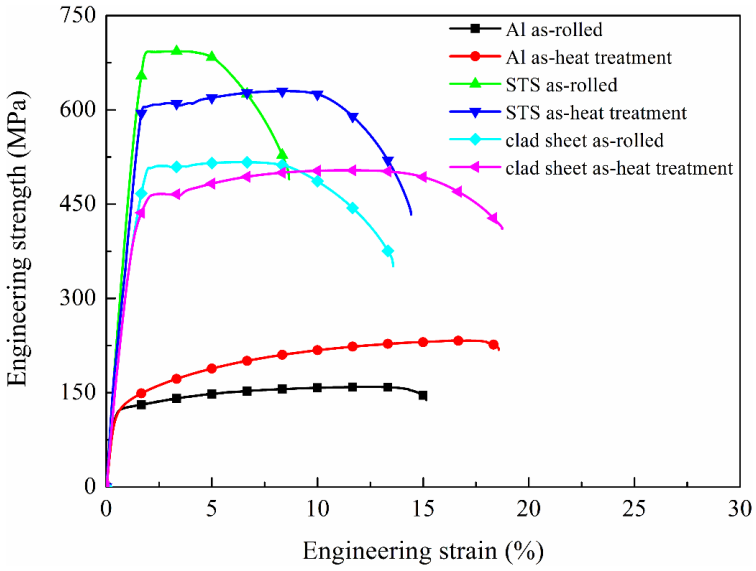


Figure 8. Engineering stress–strain curves for individual sheets and Al/steel composites.

Table 3. Tensile performances of the clad sheets and individual sheets.

Test Sample	Test Sheet	UTS (MPa)	YS (MPa)	EL (%)
Initial sample	Clad sheet	516	510	13.52
	Al	159	117	15.15
	Steel	693	687	8.63
Aged sample	Clad sheet	503	465	18.82
	Al	232	118	18.59
	Steel	630	605	14.38

The UTS and YS values of the Al/steel composites could be computed using the rule of mixture (ROM) [18,28,29]: $\sigma = \sigma_{Al} f_{Al} + \sigma_{steel} f_{steel}$, σ denoted the UTS and YS values, and f was the volume fraction of individual materials. Because of the same surface region, the volume fraction used in the rule was equal to the thickness ratio of the individual metal layer. In this study, f_{steel} had a thickness ratio of 68.62%, while that of f_{Al} was 31.38%.

Figure 9 exhibits the tensile strength values of initial and aged Al/steel composites, and the individual Al and steel layers. Compared with the UTS and YS from the experimental test of the composites, the values computed by the ROM were also plotted. The decreasing UTS and YS of the aged clad sheet was related to the recovery of steel layer. However, due to the precipitation strengthening, the aged Al alloy had a higher UTS value. Therefore, the difference in the UTS values between the initial and the aged clad sheets was less than that of the YS values. The yield ratio of the initial clad sheet was 98.83%, and that of the aged clad sheet was 92.44%. Generally, the lower yield ratio was beneficial for the moulding process of the sliding bearing material. The UTS and YS values from experimental test of the composites were consistent with the computed data according to the UTS and YS values of individual Al and steel materials. The tensile strength values of the Al/steel clad sheets followed the ROM. The tiny difference between the YS value obtained from the experiment and the YS value computed via ROM was associated with the higher interfacial bonding strength of the aged composites.

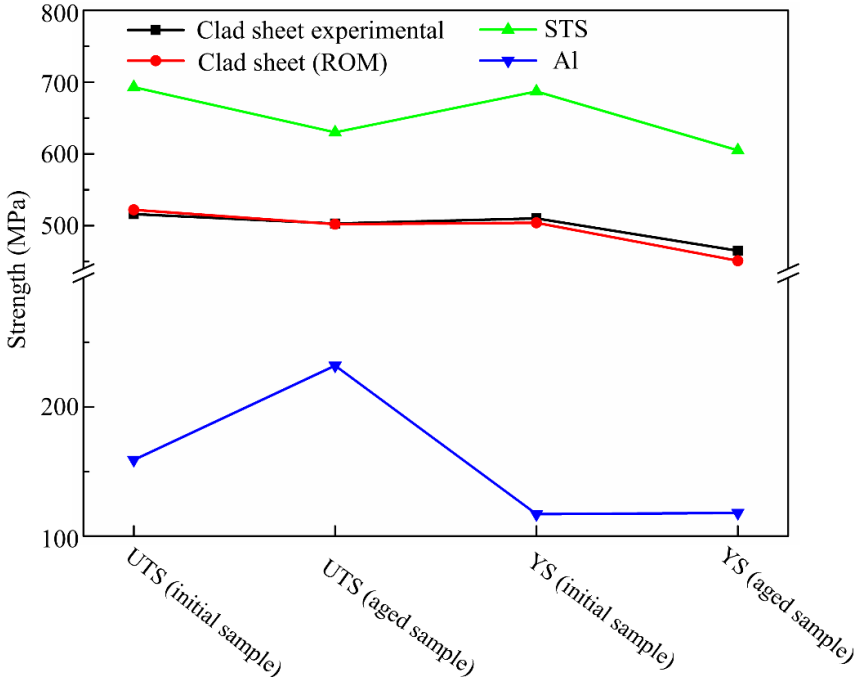


Figure 9. UTS and YS values of initial and aged Al/steel composites, and the individual Al and steel layers.

3.3. Bonding Strength of AlZn4SiPb/Steel Interface

The bonding quality of the Al/steel interface zone is one of the most important mechanical properties of clad sheets. It was obtained via the tensile shear test. The interfacial bonding strength of the initial sample was 70 MPa, and that of the aged sample was 130 MPa. Figure 10 shows the cross section of tensile shear fracture for the initial and aged samples. Two different regions were observed, as shown in Figure 10a. One region is the Al/steel interfacial zone (as marked in red arrow), and the other region is only the steel layer (as marked in blue arrow). However, only the Al/steel interfacial zone was observed, as shown in Figure 10b. The difference of fracture between the initial and aged samples was mainly related to the bonding strength of Al/steel interface. Due to the lower interfacial bonding strength of initial sample, some zone of no Al layers existed on the tensile shear fracture of steel side. It indicated the part fracture formed in the Al/steel interface. On the contrary, the higher bonding strength of the aged sample contributed to the fracture of the Al matrix. It indicated that the fracture only formed in the Al layer rather than Al/steel interface.

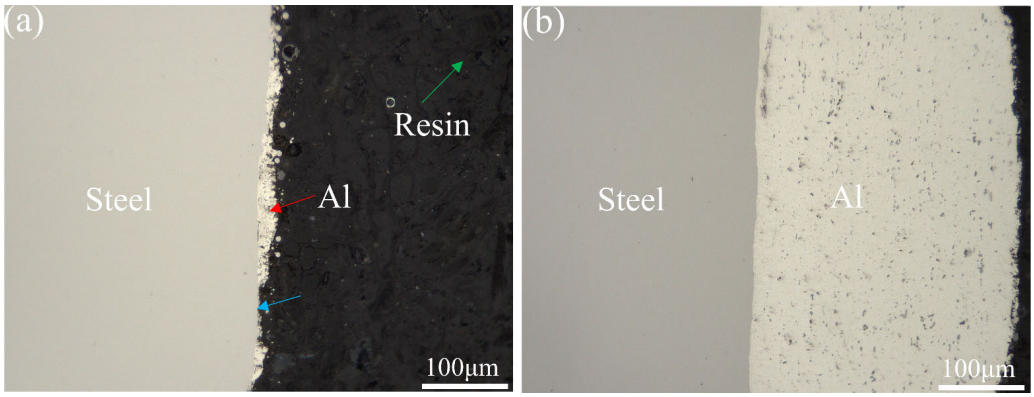


Figure 10. Cross section of tensile shear fracture: (**a**) initial sample and (**b**) aged sample.

To explore the fracture mechanism more deeply, the microstructure of fracture surface for the steel layer was characterized by SEM. Figure 11 shows the BSE images and the EDS point energy spectrum of the initial and the aged, fractured surfaces of the steel side. Three significant contrast phases can be observed in Figure 11a. Some SEM-EDS point energy spectrums were executed in the points (1–3), as illustrated in Figure 11b. The corresponding results are shown in Figure 11e–g. The three phases included Al, Pb and Fe. However, only two contrast phases were observed in Figure 11c–d. The corresponding EDS results exhibited the phases of Al and Pb.

Some zones consisting of the Fe element were observed in the fractured surface of the initial steel layer, indicating that the fracture occurred at the partial Al/steel interface. Only Al and Pb phases were observed in the cracked surface of the aged steel side, indicating that the Al/steel interface attained a high bonding strength and fracture occurred in the Al matrix. It was previously found that atom diffusion contributed to improving interfacial bonding strength [30,31]. The diffusion distance of the aged sample was 30–150 nm, as shown in Figure 5. The thin diffusion zone formed a fine metallurgical bonding and improved the interfacial bonding strength of AlZn4SiPb/steel composites [32,33]. Therefore, the aged Al alloy cracked in the tensile shear process.

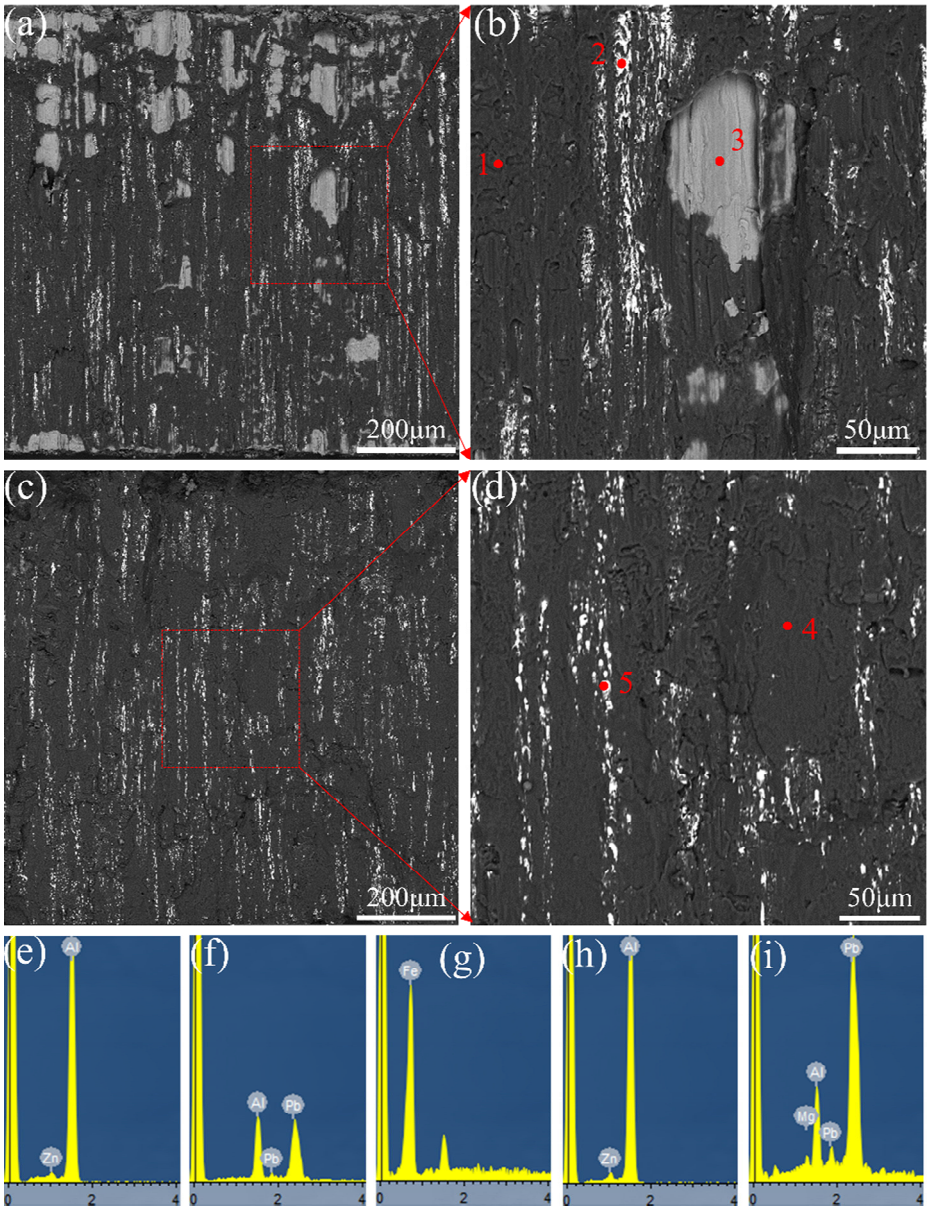


Figure 11. Fractured surfaces of steel layers and corresponding EDS point energy spectrum of Al/steel clad sheets: (**a**,**b**,**e**–**g**, respectively) initial sample and (**c**,**d**,**h**,**i**, respectively) aged sample.

4. Conclusions

The AlZn4SiPb/steel clad composite was successfully prepared via roll bonding at the room temperature. Microstructures were observed, and the mechanical performance of the composite was investigated. The main conclusions drawn from this study are as follows:

(1) The AlZn4SiPb/steel clad sheets demonstrate a satisfactory interfacial bonding. An uneven interfacial transition area with a thickness of 30–150 nm was observed in the aged sample.

(2) The Pb of the aged Al matrix is spheroidized and uniformly dispersed. Some rod-shaped nanoscale β' phases were observed in the aged Al matrix.

(3) After the solution and aging treatment, the tensile strength of the individual metal of steel layer decreased, while that of the individual Al layer increased. Moreover, the γ-fibre texture of the steel layer improved.

(4) In contrast, the aged sample has a lower yield ratio than that of the initial clad composite. The UTS and YS values of the composites are consistent with the computed

values from the ROM. The interfacial bonding strength of the initial sample is 70 MPa, while that of the aged sample is 130 MPa.

Author Contributions: Conceptualization, Q.T.; methodology, P.W.; validation, N.Z. and L.T.; formal analysis, W.H.; investigation, Y.L.; resources, Y.C.; data curation, J.S.; writing—original draft preparation, P.W. and C.L.; writing—review and editing, Z.C.; funding acquisition, Q.T. All authors have read and agreed to the published version of the manuscript.

Funding: This research was funded by the National Natural Science Foundation of China (Grant No:51975073).

Data Availability Statement: Not applicable.

Conflicts of Interest: The authors declare no conflict of interest.

References

1. Lucchetta, M.; Saporiti, F.; Audebert, F. Improvement of surface properties of an Al–Sn–Cu plain bearing alloy produced by rapid solidification. *J. Alloys Compd.* **2019**, *805*, 709–717. [CrossRef]
2. Rusin, N.M.; Skorentsev, A.L.; Krinitcyn, M.G.; Dmitriev, A.I. Tribotechnical properties of sintered antifriction aluminum-based composite under dry friction against steel. *Materials* **2022**, *15*, 180. [CrossRef]
3. Geng, H.; Ma, J. Friction and wear of AlZnPb bearing alloy. *Wear* **1993**, *169*, 201–207.
4. Cui, G.M.; Li, X.X.; Zeng, J.M. Research on Cold-Rolled Bimetal of High-Tin Aluminum Alloy and Steel. *Appl. Mech. Mater.* **2012**, *217–219*, 395–399. [CrossRef]
5. Wang, P.; Chen, Z.; Hu, C.; Li, B.; Mo, T.; Liu, Q. Effects of annealing on the interfacial structures and mechanical properties of hot roll bonded Al/Mg clad sheets. *Mater. Sci. Eng. A* **2020**, *792*, 139673. [CrossRef]
6. Zhang, H.; Niu, T.; Li, Y.; Yuan, M. Influence of high magnetic field-thermal coupling processing on diffusion bonding prop-erties and element diffusion of 1420 Al-Li Alloy. *Crystals* **2022**, *12*, 1508. [CrossRef]
7. Yang, M.; Ma, H.-H.; Shen, Z.-W.; Chen, D.-G.; Deng, Y.-X. Microstructure and mechanical properties of Al-Fe meshing bonding interfaces manufactured by explosive welding. *Trans. Nonferrous Met. Soc. China* **2019**, *29*, 680–691. [CrossRef]
8. Deepika, D.; Anitha Lakshmi, A.; Srinivasa Rao, C.; Sateesh, N.; Nookaraju, B.C.; Subbiah, R. Formability of tailor welded blanks of aluminium alloy and steel-review. *Mater. Today Proc.* **2021**, *46*, 722–728. [CrossRef]
9. Fu, L.; Xiao, H.; Yu, C.; Lv, Q.; Zhang, S.; Xie, H. Bonding enhancement of cold rolling Al/steel composite plates via self-nano film modification. *J. Mater. Process. Technol.* **2021**, *300*, 117427. [CrossRef]
10. Lanzutti, A.; Lekka, M.D.; Leitenburg, C.; Fedrizzi, L. Effect of pulse current on wear behavior of Ni matrix micro-and nano-SiC composite coatings at room and elevated temperature. *Tribol. Int.* **2019**, *132*, 50–61. [CrossRef]
11. Tseluikin, V.N.; Koreshkova, A.A. Pulsed Electrodeposition of Composite Coatings Based on Zinc–Nickel Alloy. *Prot. Met. Phys. Chem. Surfaces* **2018**, *54*, 453–456. [CrossRef]
12. Chen, K.; Liu, W.W.; Wang, T.; Wang, N.J.; Chen, Z.Y. Experimental research on the technology of two-pass different temperature rolling for thick steel/aluminum/aluminum alloy composite plate. *Int. Adv. Manuf. Technol.* **2022**, *120*, 7689–7705. [CrossRef]
13. Filho, A.A.M.; Timokhina, I.; Molotnikov, A.; Hodgson, P.D.; Lapovok, R. Role of shear in interface formation of Aluminium-Steel multilayered composite sheets. *Mater. Sci. Eng. A* **2017**, *705*, 142–152.
14. Kim, Y.K.; Hong, S.I. Influence of interface structure and stress distribution on fracture and mechanical performance of STS439/Al1050/STS304 clad composite. *Mater. Sci. Eng. A* **2019**, *749*, 35–47. [CrossRef]
15. Chen, G.; Xu, G.M. Interfacial reaction in twin-roll cast AA1100/409L clad sheet during different sequence of cold rolling and annealing. *Met. Mater. Int.* **2021**, *27*, 3013–3025. [CrossRef]
16. Silva, A.P.; Garcia, A.; Spinelli, J.E. Microstructural Morphologies and Experimental Growth Laws during Solidification of Monotectic and Hypermonotectic Al–Pb Alloys. *J. Mater. Sci. Technol.* **2014**, *30*, 401–407. [CrossRef]
17. Mohau, S.; Agarvvala, V.; Ray, S. The effect of lead content on the wear characteristics stir-cast Al-Pb alloy. *Wear* **1990**, *140*, 83–92.
18. Wang, P.; Chen, Z.; Hu, C.; Li, B.; Lin, J.; Liu, Q. Effects of annealing on the interface microstructures and mechanical properties of hot roll bonded Ti6Al4V/AA6061 clad sheets. *J. Mater. Res. Technol.* **2020**, *9*, 11813–11825. [CrossRef]
19. Hirano, K.-I.; Agarwala, R.; Cohen, M. Diffusion of iron, nickel and cobalt in aluminum. *Acta Met.* **1962**, *10*, 857–863. [CrossRef]
20. Yang, Y.; Zhang, F.; He, J.; Qin, Y.; Liu, B.; Yang, M.; Yin, F. Microstructure, growth kinetics and mechanical properties of interface layer for roll bonded aluminum-steel clad sheet annealed under argon gas protection. *Vacuum* **2018**, *151*, 189–196. [CrossRef]
21. Sagalowicz, L.; Lapasset, G.; Hug, G. Transmission electron microscopy study of a precipitate which forms in the Al-Mg-Si system. *Philos. Mag. Lett.* **1996**, *74*, 57–66. [CrossRef]
22. Zhu, Q.; Cao, L.; Wu, X.; Zou, Y.; Couper, M.J. Effect of Ag on age-hardening response of Al-Zn-Mg-Cu alloys. *Mater. Sci. Eng. A* **2019**, *754*, 265–268. [CrossRef]
23. Wolverton, C. Crystal structure and stability of complex precipitate phases in Al-Cu-Mg-(Si) and Al-Zn-Mg alloys. *Acta. Mater.* **2001**, *49*, 3129–3142. [CrossRef]

24. Guo, M.X.; Zhang, X.K.; Zhang, J.S.; Zhuang, L.Z. Effect of Zn addition on the precipitation behaviors of Al-Mg-Si-Cu alloys for automotive applications. *J. Mater. Sci.* **2017**, *52*, 1390–1404. [CrossRef]
25. Mao, H.; Bai, X.; Song, F.; Song, Y.; Jia, Z.; Xu, H.; Wang, Y. Effect of Cd on mechanical properties of Al-Si-Cu-Mg alloys un-der different multi-stage solution heat treatment. *Materials* **2022**, *15*, 5101. [CrossRef] [PubMed]
26. Tikhovskiy, I.; Raabe, D.; Roters, F. Simulation of the deformation texture of a 17%Cr ferritic stainless steel using the texture component crystal plasticity finite element method considering texture gradients. *Scr. Mater.* **2006**, *54*, 1537–1542. [CrossRef]
27. Yan, H.; Bi, H.; Li, X.; Xu, Z. Microstructure, texture and grain boundaries character distribution evolution of ferritic stainless steel during rolling process. *J. Mater. Process. Technol.* **2009**, *209*, 2627–2631. [CrossRef]
28. Chen, W.; He, W.; Chen, Z.; Jiang, B.; Liu, Q. Extraordinary room temperature tensile ductility of laminated Ti/Al composite: Roles of anisotropy and strain rate sensitivity. *Int. J. Plast.* **2020**, *133*, 102806. [CrossRef]
29. Liu, K.; Sheng, X.; Li, Q.; Zhang, M.; Han, N.; He, G.; Zou, J.; Chen, W.; Atrens, A. Microstructure and Strengthening Model of Cu–Fe In-Situ Composites. *Materials* **2020**, *13*, 3464. [CrossRef]
30. Li, B.; Chen, Z.; He, W.; Wang, P.; Lin, J.; Wang, Y.; Peng, L.; Li, J.; Liu, Q. Effect of interlayer material and rolling temperature on microstructures and mechanical properties of titanium/steel clad plates. *Mater. Sci. Eng. A* **2019**, *749*, 241–248. [CrossRef]
31. Yang, B.; Li, Z.; Fan, K.; Liu, B.; Yu, W.; Yin, F. Warm Rolled Temperature Effect on Microstructure and Mechanical Properties of 18Mn/40Si2CrMo Multilayer Composite Steel. *Crystals* **2022**, *12*, 1652. [CrossRef]
32. Lee, K.S.; Bae, S.J.; Lee, H.W.; Kang, S.H. Interface-correlated bonding properties for a roll-bonded Ti/Al 2-ply sheet. *Mater. Charact.* **2017**, *134*, 163–171. [CrossRef]
33. Wang, P.; Huang, H.; Liu, J.; Lin, J.; Liu, Q.; Chen, Z. Microstructure and mechanical properties of Ti6Al4V/AA6061/AZ31 laminated metal composites (LMCs) fabricated by hot roll bonding. *J. Alloys Compd.* **2020**, *861*, 157943. [CrossRef]

Disclaimer/Publisher's Note: The statements, opinions and data contained in all publications are solely those of the individual author(s) and contributor(s) and not of MDPI and/or the editor(s). MDPI and/or the editor(s) disclaim responsibility for any injury to people or property resulting from any ideas, methods, instructions or products referred to in the content.